

# SUPPLEMENTAL MATERIAL

## Dynamic Similarity of Oscillatory Flows Induced by Nanomechanical Resonators

Elizabeth C. Bullard<sup>1</sup>, Jianchang Li<sup>2</sup>, Charles R. Lilley<sup>3</sup>, Paul Mulvaney<sup>2</sup>, Michael L. Roukes<sup>2</sup> and John E. Sader<sup>1,3\*</sup>

<sup>1</sup>*Kavli Nanoscience Institute and Departments of Physics, Applied Physics, and Bioengineering, California Institute of Technology, Pasadena, California 91125*

<sup>2</sup>*School of Chemistry and Bio21 Institute, The University of Melbourne, Victoria 3010, Australia*

<sup>3</sup>*Department of Mathematics and Statistics, The University of Melbourne, Victoria 3010, Australia*

### 1. Derivation of Equation (4) in the Main Text

The dynamic similarity theorem in Eq. (7) is derived from Eq. (4). Equation (4) is obtained by extending the dimensional analysis of Refs. [1, 2] to include an extra physical quantity, the gas mean free path. Here, we provide the details of the derivation of Eq. (4). The principal assumptions are:

- (1) The resonator behaves as a linearly elastic solid;
- (2) Energy dissipation due to vibration occurs in the gas;
- (3) The oscillation amplitude of the resonator is small, so that all nonlinearities due to the resonator and gas are negligible.

The maximum energy stored in the resonator directly follows:

$$E_{\text{stored}} = \frac{1}{2} k A^2, \quad (\text{S1})$$

where  $k$  is the resonator stiffness, and  $A$  is the oscillation amplitude. The energy dissipated in the gas can be quantified by the (dimensionless) quality factor,

$$Q \equiv 2\pi \left. \frac{E_{\text{stored}}}{E_{\text{diss}}} \right|_{\omega=\omega_R}, \quad (\text{S2})$$

where  $E_{\text{diss}}$  is the energy dissipated per oscillation cycle, at the radial resonant frequency  $\omega_R$ .

Since the flow is linear, the energy dissipated in the gas per oscillation cycle depends on the square of the oscillation amplitude,  $A$ . From Eqs. (S1) and (S2), we then obtain

$$k = \left( \frac{1}{2\pi} \left. \frac{\partial^2 E_{\text{diss}}}{\partial A^2} \right|_{\omega=\omega_R} \right) Q, \quad (\text{S3})$$

which is independent of the oscillation amplitude.

In accord with the above-listed assumptions, the energy dissipated per cycle  $E_{diss}$  must depend on (i) the square of the resonator's oscillation amplitude,  $A$ , (ii) the gas density  $\rho$  and shear viscosity  $\mu$ , (iii) the gas mean free path  $\lambda$ , (iv) the linear dimension (size) of the resonator, denoted  $L_0$ , (v) the relevant frequency of oscillation, which from Eq. (S3) is the resonant frequency in gas,  $\omega_R$ , (vi) the mode shape of the resonator, and (vii) its geometry. Note that the last two quantities are dimensionless.

The functional form of  $E_{diss}$ , in terms of these parameters, can be rigorously determined using dimensional analysis [3]. It follows that the product

$$\rho^m \mu^n L_0^p \omega_R^q \lambda^r \left( \frac{1}{2\pi} \frac{\partial^2 E_{diss}}{\partial A^2} \Big|_{\omega=\omega_R} \right), \quad (S4)$$

must be dimensionless, where  $m, n, p, q, r$  are constants to be evaluated. Equating dimensions in Eq. (S4) leads to three independent dimensionless groups:

$$\Pi \equiv \frac{1}{\rho L_0^3 \omega_R^2} \left( \frac{1}{2\pi} \frac{\partial^2 E_{diss}}{\partial A^2} \Big|_{\omega=\omega_R} \right), \quad \text{Re} \equiv \frac{\rho L_0^2 \omega_R}{\mu}, \quad \text{Kn} = \frac{\lambda}{L_0}. \quad (S5)$$

The second and third parameters are commonly referred to as the Reynolds and Knudsen numbers, respectively.

From Buckingham's  $\pi$  theorem [3], it follows that there must exist a function,

$$H \left( \frac{1}{\rho L_0^3 \omega_R^2} \left( \frac{1}{2\pi} \frac{\partial^2 E_{diss}}{\partial A^2} \Big|_{\omega=\omega_R} \right), \frac{\rho L_0^2 \omega_R}{\mu}, \frac{\lambda}{L_0} \right) = 0, \quad (S6)$$

which relates the energy dissipated per cycle  $E_{diss}$  to all other parameters. Solving Eq. (S6) for the first argument and rearranging gives

$$\frac{1}{2\pi} \frac{\partial^2 E_{diss}}{\partial A^2} \Big|_{\omega=\omega_R} = \rho L_0^3 \omega_R^2 \Omega(\text{Re}, \text{Kn}), \quad (S7)$$

where the dimensionless function  $\Omega(\text{Re}, \text{Kn})$  is to be determined. Substituting Eq. (S7) into Eq. (S3) gives

$$k = \rho L_0^3 \Omega(\text{Re}, \text{Kn}) \omega_R^2 Q, \quad (S8)$$

which is the required expression, Eq. (4), of the main text.

## 2. Device Fabrication

We used 4" silicon wafers coated with 100nm, 300nm, or 500nm of low stress silicon nitride (SiN) on both sides to fabricate the devices. Photolithography was used to define etch windows on the backside of each wafer, followed by a dry etch to remove the SiN. A KOH etch removed the silicon from the selected areas to form SiN membranes on the front side of the wafer. Electron beam lithography was used to define cantilevers on the edges of the membranes. We deposited either a layer of Cr or a Cr/Au layer as an etch mask. We dry etched the silicon nitride membranes to define the cantilevers. We then removed the metal layer(s) with a wet etch. All of the devices were then coated with a Cr/Au layer for reflectivity; a thermal evaporator was used for the 100nm and 500nm devices, while an electron beam evaporator was used for the 300nm devices. Prior to deposition of the metal layer on the devices, we performed a test deposition on a SiN coated SOI wafer, patterned with rectangles with photolithography. After liftoff, we measured the step height of the metal layer with an atomic force microscope. The step height was used to calibrate the subsequent deposition on the devices. The 500nm devices have a 3nm layer of Cr with a 100-110nm thick layer of Au on top. The 300nm devices have a 3nm layer of Cr with a 60-66nm layer of Au on top. The 100nm devices have a 3nm layer of Cr with a 20-22nm layer of Au on top. The reflective layer was not deposited prior to the etch of the SiN membrane because the etch would have also etched the Au, leaving a layer of unknown thickness. The thickness of the metal layers must be with 10% of the desired thickness to ensure geometric similarity between the devices, as well ensuring that the density of the devices remains constant. Images of the 100nm set of devices are shown in Figure S1.

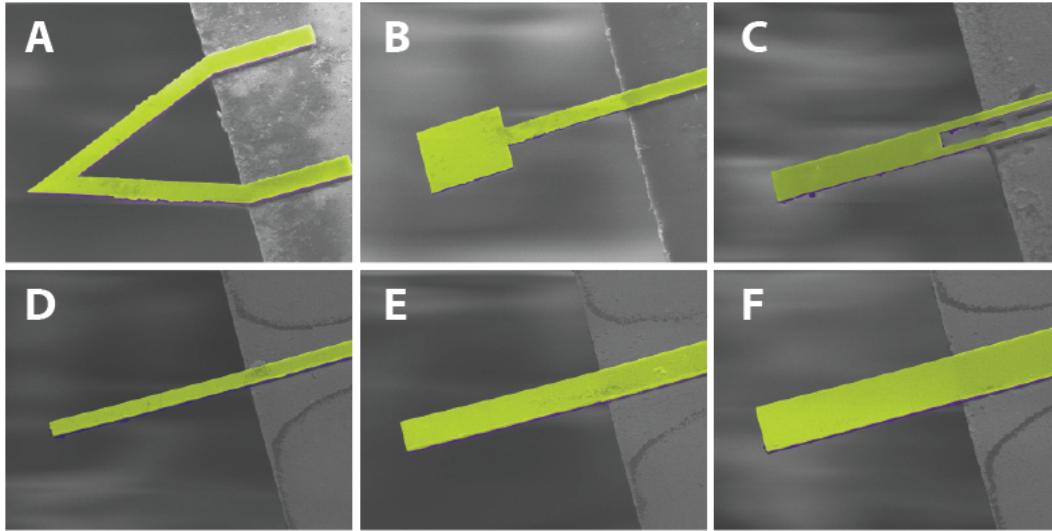


**Figure S1:** SEM micrographs (colorized for clarity) of 100nm devices, of length  $L = 10\mu\text{m}$ . Yellow is gold; purple is SiN. All images are taken at 7500x magnification. Devices labeled in accordance with Figure 1. A: Triangular cantilever; B: (a) Square paddle head cantilever; C: Cantilever with legs; D: length/width=10 rectangular cantilever; E: length/width=5 rectangular cantilever; F: length/width=3 rectangular cantilever.

### 3. Experimental Setup

We used optical interferometry to measure the quality factors of the devices with both a network analyzer and a spectrum analyzer. We placed the devices in chamber and changed the pressure from 3mT to 760T.

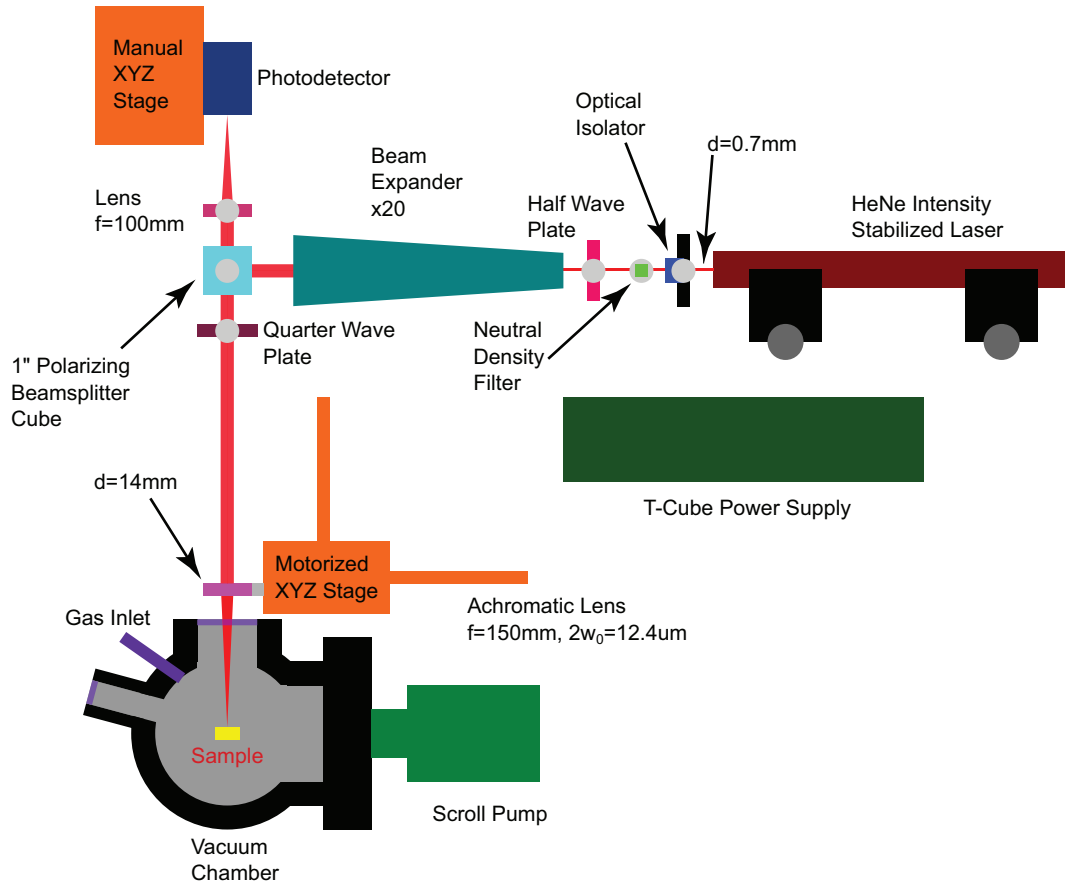


**Figure S2:** Schematic of apparatus used for gas pressure measurements of cantilever devices.

#### Optical Interferometry

A picture of the optical setup is shown in Figure S2. The simple interferometer is very similar to the design used by Rugar *et al.* [4]. The first component of the detection system is the laser. We used an amplitude stabilized HeNe laser to minimize fluctuations in the beam intensity. Fluctuations in the intensity of the laser are indistinguishable from fluctuations caused by a change in the path length; consequently, the amplitude stabilization reduces the noise. Following the laser is an optical isolator, which prevents any light reflected from components further along the beam path from entering the laser; the reflected light could destabilize the laser. The next component is a half wave plate in a

rotation mount; the polarization is adjusted for the maximum amount of light to enter the interferometer. Following the half wave plate is a neutral density filter, used to attenuate the beam power. We used a ND=1.5 filter while making measurement for the 500nm and 300nm devices and a ND=1.0 filter while making measurements for the 100nm devices. We chose these levels of attenuation to limit heating of the device under measurement, in order to prevent drift in the resonant frequency. A 20× beam expander follows. When the beam exits the laser, it has a  $1/e^2$  diameter of 0.7mm. The 20× beam expander increases the  $1/e^2$  diameter to 14mm; the beam expander is required to minimize the spot size at the sample. The minimum spot size at the sample,  $2w_0$ , is set by the diffraction limit. The minimum spot size is given in Equation 1 [5]:

$$2w_0 = 1.83 \frac{f\lambda}{D}, \quad (\text{S9})$$

where  $f$  is the focal length of the lens,  $\lambda$  is the wavelength of light, and  $D$  is the diameter of the input beam. Due to constraints on the diameter of the vacuum chamber, the minimum focal length of the lens is 150mm, which corresponds to a spot size of 12.4 $\mu$ m at the sample.

The next component in the optical setup is the polarizing beam splitter cube. The PBS splits the beam into its two orthogonal polarization components. The PBS also prevent ghost reflections, which would occur with a plate beam splitter. Following the PBS is a quarter wave plate in a rotation mount; the quarter wave plate is required to rotate the polarization of the beam by 90° so that the beam reflected from the sample is directed to the photodetector. The light is then focused through an achromatic lens mounted in a kinematic mirror mount on a motorized XYZ stage. We have chosen an achromatic lens to reduce aberrations in the beam. The lens is also chosen to ensure the highest numerical aperture possible. The XYZ stage is used to move the beam during alignment.

The beam then enters the vacuum chamber through a quartz window with an anti-reflective coating. A portion of the beam hits the device and is reflected back along the optical path until it reaches the PBS, where it is directed to the photodetector. The remainder of the beam is reflected by the piezoshaker underneath the chip containing the cantilevers. Prior to entering the photodetector, the beam traverses a lens with a focal length of 100mm, to reduce the beam size, since the diameter of the active area of the photodetector is 0.8mm. The photodetector is a New Focus 1801 photodetector, which has a bandwidth of DC-125MHz and a noise floor of 3.3 pW/ $\sqrt{\text{Hz}}$ . The photodetector is mounted on an XYZ translation stage for alignment with the beam.

## Measurements

We measured the quality factors of the devices over a range of pressures. We measured two quantities: the intrinsic quality factor of the devices,  $Q_{\text{int}}$ , and the quality factor due to gas damping, denoted  $Q$ . We used the optical setup to detect the motion of the devices and a piezoshaker to actuate them. We mounted a piezoshaker with silver paste onto a PCB and then mounted the chip containing the cantilevers to the piezoshaker with superglue. We then wire bonded the piezoshaker to the PCB. We placed the device in a vacuum chamber pumped with a scroll pump with a base pressure of  $\approx 3$  mT. We varied the pressure in the chamber by adding  $\text{N}_2$  gas through a needle valve attached to the chamber. We measured the pressure with a MKS 317 Pirani gauge, accurate to 1% of the indicated decade, with two digits of precision.

We measured the intrinsic quality factor,  $Q_{\text{int}}$ , of each device at a few mT with an Agilent 4395A Network/Spectrum/Impedance Analyzer in network analyzer mode. We drove the devices with the piezoshaker and measured the photodetector output. We used a network analyzer to measure  $Q_{\text{int}}$  because measurements of the thermomechanical noise spectrum with the 4395A in spectrum analyzer mode had a variance of about 10%-15% of the measured quality factor. Such inconsistent measurements would require several (about 10) measurements to acquire an accurate value for the quality factor. An accurate value for the intrinsic quality factor,  $Q_{\text{int}}$ , is required to convert the measured (total) quality factor  $Q_{\text{total}}$  at larger gas pressures to the quality factor due to gas damping,  $Q$ ;

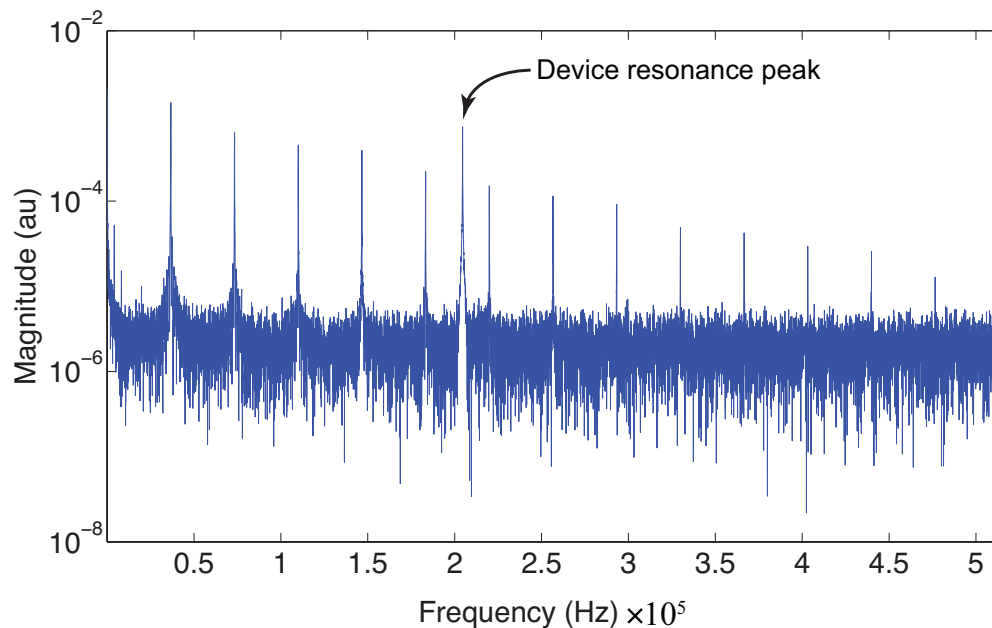


**Figure S3:** FFT of piezoshaker excited device showing resonance peak and laser noise peaks.

see Section 4. The measurements made with the network analyzer had a variance of less than 1%, leading to significantly faster measurements. We fitted the resonance peak to the response of a damped harmonic oscillator using a non-linear least squares fit in MATLAB.

However, we were unable to use the NA to make the quality factor vs pressure measurements because both the response of the piezoshaker at higher pressures and laser noise altered the shape of the response, rendering it no longer a Lorentzian. The thermomechanical noise spectrum measured with the SA was always Lorentzian, occasionally with peaks from the laser noise. The laser noise is present even when the beam splitter is replaced with a mirror to directly send the beam to the photodetector. The laser has noise peaks at the following frequencies in kHz: 36.7, 73.3, 110, 147, 183, 220, 257, 293, 330, 367, 403, 440, 477. A fast Fourier transform of a ring down measurement collected with an Agilent 54845A oscilloscope for a cantilever with a resonant frequency of 204.6kHz is shown in Figure S3; the laser noise peaks are clearly visible. We could easily remove the peaks from the laser noise during the fitting of the thermomechanical noise spectrum. The thermomechanical displacement noise spectral density for a cantilever is given by Equation 2 [6]:

$$S_x^{th}(\omega) = \frac{\omega_R}{(\omega_R^2 - \omega^2)^2 + (\omega_R \omega / Q_{total})^2} \frac{4k_B T}{M_{eff} Q_{total}}, \quad (S10)$$

where  $\omega_R$  is the radial resonant frequency of the cantilever,  $Q_{total}$  is the measured quality factor (due to all dissipation processes present),  $k_B$  is Boltzmann's constant,  $T$  is the temperature, and  $M_{eff}$  is the

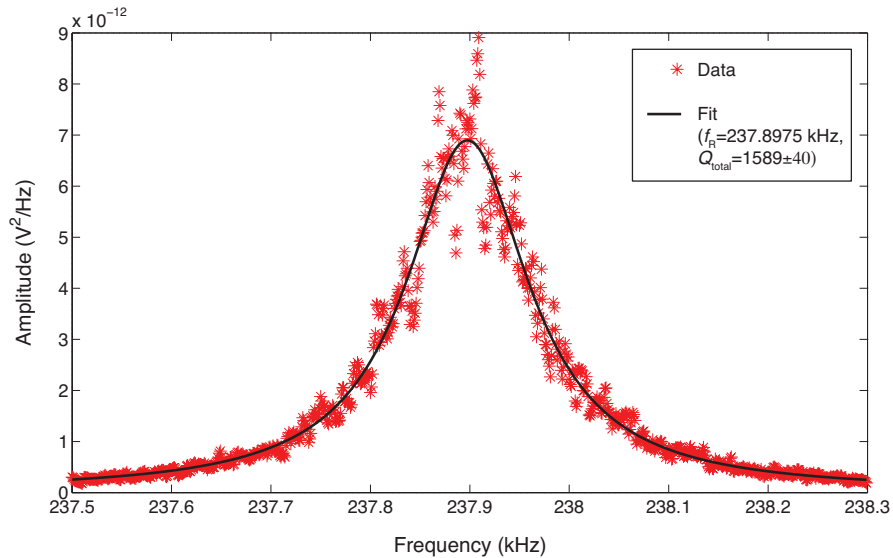


**Figure S4:** Thermomechanical noise spectrum for Device E, thickness 500nm, Run 1, showing fit to Eq. (S10).

effective mass of the cantilever. For a cantilever with an aspect ratio  $L/b > 3$ ,  $M_{\text{eff}} \approx 0.24M$  [7]. Shown in Figure S4 is the thermomechanical noise peak for Device E with thickness 500nm, Run 1, at  $P = 3.7\text{mT}$ .

We fitted the thermomechanical noise peak to Eq. (S10) using a non-linear least squares fit in MATLAB; see Figure S4. We measured quality factor  $Q_{\text{total}}$  vs pressure for each device with the spectrum analyzer, with three measurements below 10mT. The rest of the measurements were logarithmically spaced for four measurements each decade, with the exception of 100T-1000T; the measurement was terminated at 760T. For the 500nm devices, a measurement was made at 150T instead of 170T to enable comparison with the quality factor of the 100nm devices at 760T. For the 300nm devices, an additional measurement was made at 250T for the same reason. Figure S5a shows the thermomechanical noise peak for Device D measured at  $P = 1\text{T}$ . Figure S5b gives the measured quality factor  $Q_{\text{total}}$  vs pressure for a measurement run on this device, as well as frequency  $f_R$  vs pressure in an inset to verify the assumption that  $\omega_R \approx \omega_{\text{vac}}$  for these devices. Results for all devices are given in Section 5.

Measurements were performed on two devices for each device type (A-F) and thickness (100nm, 300nm, 500nm), for a total of 36 devices. Each device was measured twice, for a total of 72 measurement runs. Results for one of each type of device are given in Figure S6, including both measurement runs. The measurements were consistent between devices and only one device of each type and thickness is included for clarity.

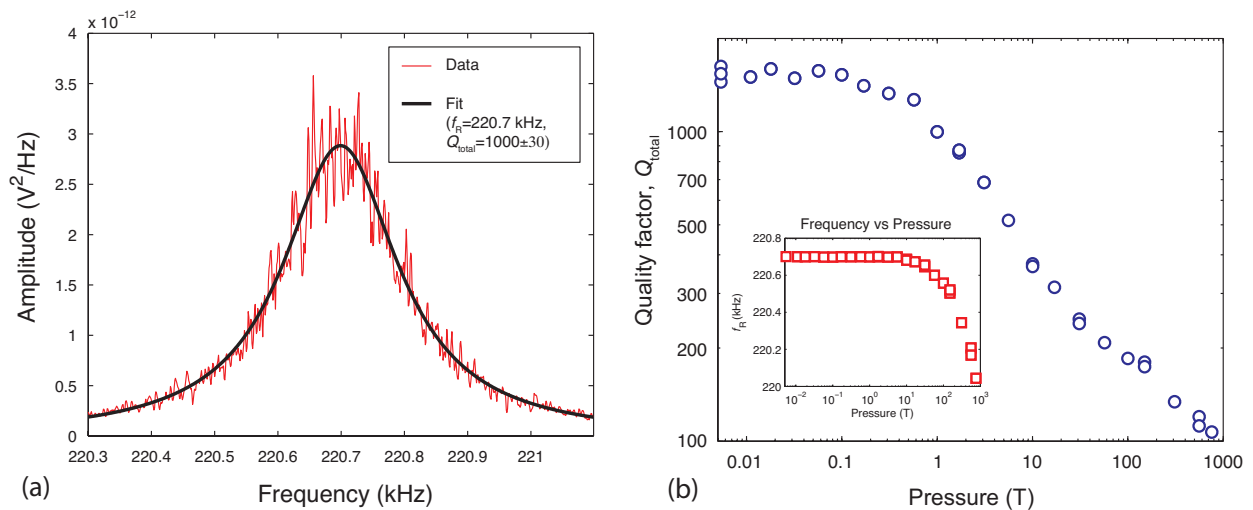


**Figure S5:** Measurement on 500nm 10:1 aspect ratio device, Device D, Run 1. (a) Fit of thermomechanical noise peak, Eq. (S10), measured at  $P = 1\text{T}$ . (b) Measured quality factor  $Q_{\text{total}}$  vs pressure, with resonant frequency  $f_R$  vs pressure shown in inset.

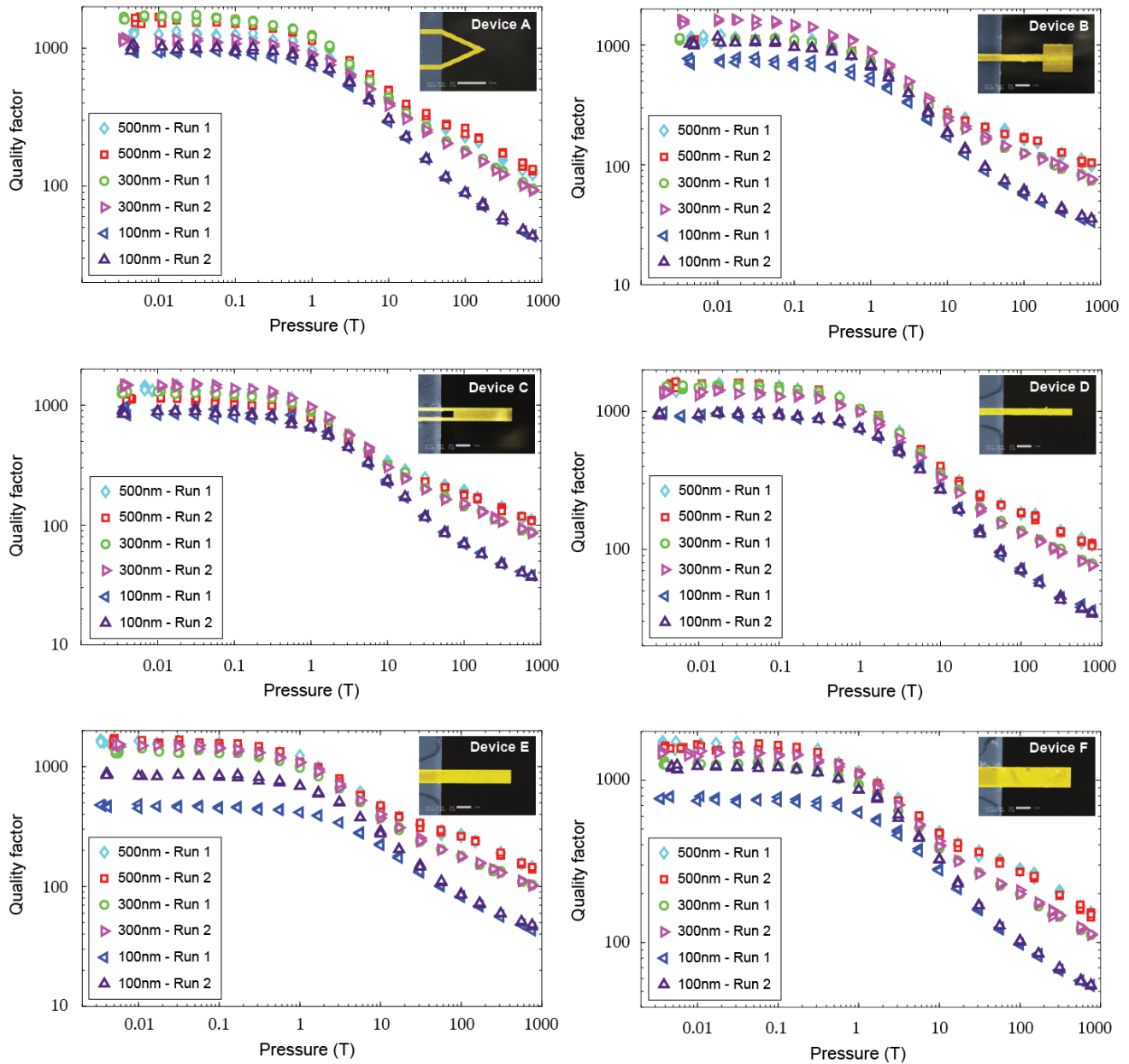


**Figure S6:** Measured quality factors,  $Q_{\text{total}}$ , as a function of gas pressure for all devices.

#### 4. Quality Factor Measurements

Measurements of the quality factors for one of each type of device (Device A-F) and thickness (100nm, 300nm, 500nm), as a function of  $N_2$  gas pressure, are given in Figure S6. The quality factors due to the gas only,  $Q$ , are obtained using the relation:

$$\frac{1}{Q_{\text{total}}} = \frac{1}{Q} + \frac{1}{Q_{\text{int}}}, \quad (\text{S11})$$

where  $Q_{\text{total}}$  is the quality factor measured in Figure S6 and  $Q_{\text{int}}$  is the measured intrinsic quality factor (at very low gas pressure), see above.

Use of Eq. (10) in Table I requires gas pressures that are intermediate to those measured for the 500 nm device. To determine  $Q$  at these gas pressures, data reported in Table I are obtained by fitting and interpolating measured data of  $Q$  vs gas pressure on a double logarithmic-scale [2]. This is performed for both the 100nm and 500nm data; see Figure S7. This fit procedure is not used elsewhere.

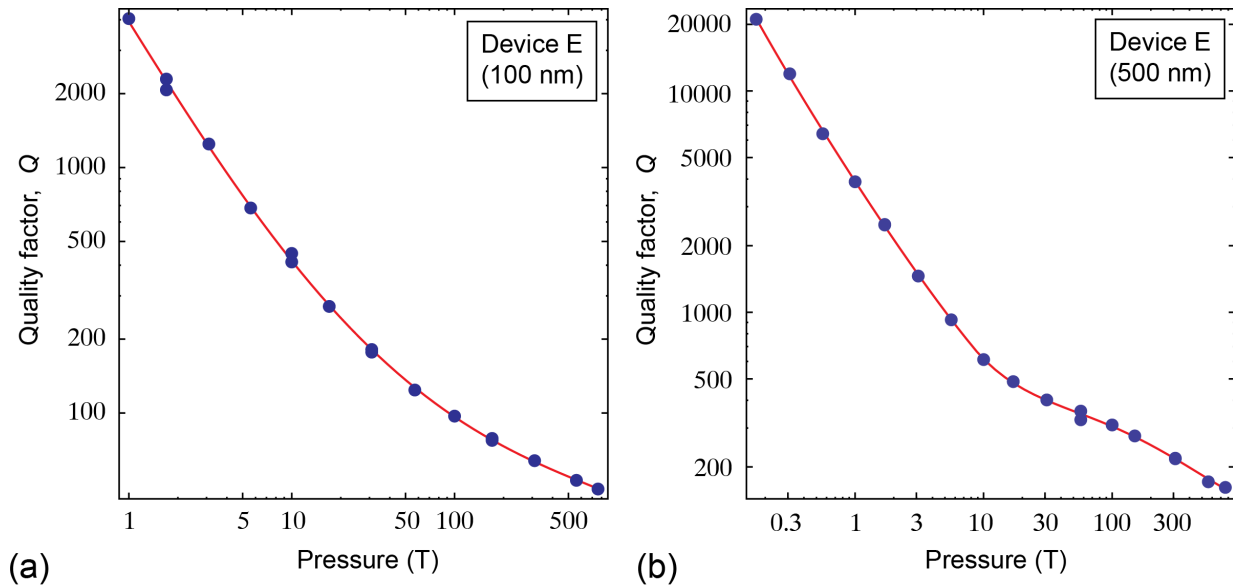


**Figure S7:** Measured quality factors,  $Q$ , vs gas pressure (dots) for Device E with fits shown [lines]. (a) 100nm device; (b) 500nm device.

The scaled quality factors,  $H(\text{Kn})$ , determined from the raw data in Figure S6 and Eq. (S11), are given in Figure S8. The chosen length scales for the Knudsen number are: Devices A, D, E, F: leg width at clamp; Devices B, C: Width at free end.

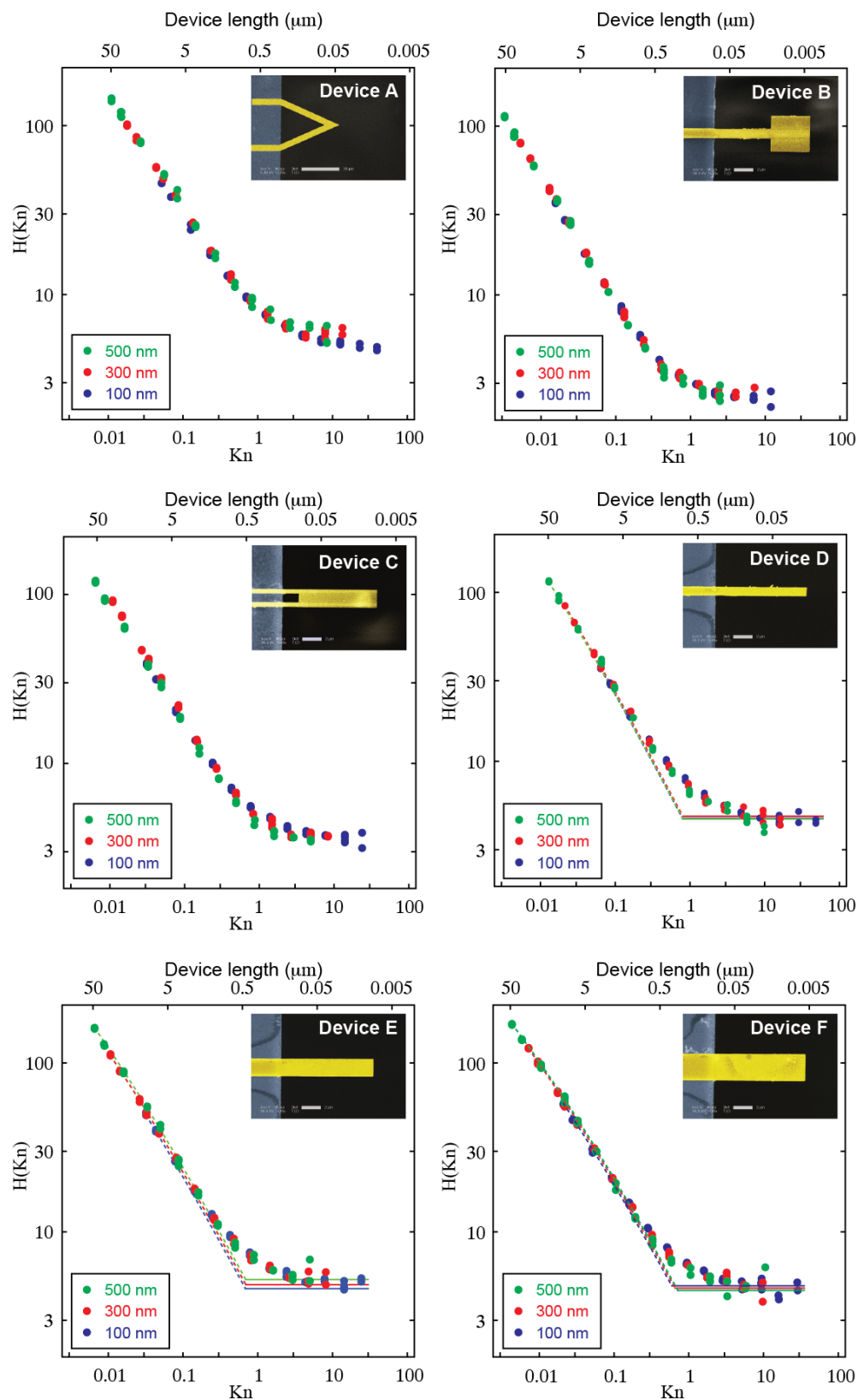


**Figure S8:** Scaled quality factor  $H(Kn)$  for all cantilever devices. Caption as for Figure 3.

## 5. Quality Factor of Rectangular Cantilever in Free Molecular Flow

Here we present an expression for the quality factor due to the gas,  $Q$ , of a rectangular cantilever immersed in gas, in the limit of free molecular flow [8, 9]. Free-molecular conditions exist when gas molecules collide with surfaces only, and not each other. This occurs in the upper limit of rarefaction, where  $\text{Kn} \rightarrow \infty$ .

We begin by considering the case of an infinitely thin rigid blade, of infinite length and width  $b$ , moving in a stationary gas. Bird [10] gives the free-molecular drag coefficient for such a blade moving at arbitrary angle of incidence to a stationary gas. At normal incidence to its face, this expression gives the following result for the normalized pressure

$$\hat{p}_{\text{FM}} \equiv \frac{p}{\rho RT} = \frac{2(1+\varepsilon)}{\sqrt{\pi}} s \exp(-s^2) + [1 + 2s^2 + \varepsilon(1 - 2s^2)] \text{erf}(s) + s(1-\varepsilon)\sqrt{\pi\hat{T}}, \quad (\text{S12})$$

where  $p$  is the gas pressure,  $\rho$  the gas density,  $R$  is the specific gas constant,  $T$  is the gas temperature far from the blade,  $T_{\text{wall}}$  is the blade temperature,  $\hat{T} \equiv T_{\text{wall}}/T$ ,  $\varepsilon$  is the specular reflection coefficient at the blade surface,  $s \equiv u_{\text{blade}}/c_{\text{mp}}$ ,  $u_{\text{blade}}$  is the blade speed, and  $c_{\text{mp}} = \sqrt{2RT}$  is a characteristic thermal speed.

Since we are only interested in the low Mach number solution, relevant to measurements on cantilever devices, we formally expand Eq. (S12) in the asymptotic limit of small  $s$ . We also consider the case where the system is in thermal equilibrium, and the blade temperature matches the free stream temperature, i.e.,  $\hat{T} = 1$ . This gives the following result for the normalized pressure at the blade surface:

$$\hat{p}_{\text{FM}} = \frac{s}{K(\varepsilon)} + O(s^3), \quad (\text{S13})$$

where

$$K(\varepsilon) = \frac{\sqrt{\pi}}{4 + \pi + (4 - \pi)\varepsilon}. \quad (\text{S14})$$

The force per unit length experienced by the rigid blade oscillating in a gas directly follows from Eq. (S13):

$$F = \frac{\rho c_{\text{mp}} b}{2K(\varepsilon)} u_{\text{blade}}. \quad (\text{S15})$$

The formalism of Ref. [11] can then be used to determine the hydrodynamic function for a

rectangular cantilever vibrating in a gas under free molecular conditions:

$$\Gamma(\omega) = \left[ \frac{2}{\pi K(\varepsilon)} \frac{c_{\text{mp}}}{\omega b} \right] i, \quad (\text{S16})$$

where  $\omega$  is the radial frequency of oscillation of the cantilever and  $i$  is the usual imaginary unit. The hydrodynamic function in Eq. (S16) is purely imaginary, indicating that the hydrodynamic load is dissipative only. Substituting Eq. (S16) into the general form for the quality factor:

$$Q = \frac{\frac{4\rho_{av}h}{\pi\rho b} + \Gamma_r(\omega_R)}{\Gamma_i(\omega_R)}, \quad (\text{S17})$$

where the subscripts  $r$  and  $i$  indicate the real and imaginary components,  $\rho_{av}$  is the average cantilever density,  $h$  is the cantilever thickness, and  $\omega_R$  is the resonant frequency of the cantilever, gives the required result for the quality factor in the free molecular flow limit:

$$Q_{FM} = \frac{K(\varepsilon)\rho_{av}h\omega_{vac}(2RT)^{1/2}}{p}. \quad (\text{S18})$$

In deriving Eq. (S18) we have used the property that the hydrodynamic load is purely dissipative, and hence the resonant frequency is identical to its value in vacuum, i.e.,  $\omega_R = \omega_{vac}$ . Note that Eq. (S18) applies formally in the limit where the cantilever width  $b$  greatly exceeds its thickness  $h$ .

## 6. Dependence of Scaled Quality Factor on Device Geometry

Dependence of the scaled quality factor on device geometry is illustrated in Figure S8, where data for all devices is plotted in a single graph. This combined plot clearly shows that the function  $H(Kn)$  depends strongly on the device geometry, with factors of 2-5 observable between different datasets. This contrasts to the high precision in which data from three sets of devices (100, 300, 500nm thicknesses) of the same type collapse onto a single curve, *cf.* Figures S8 and S9.

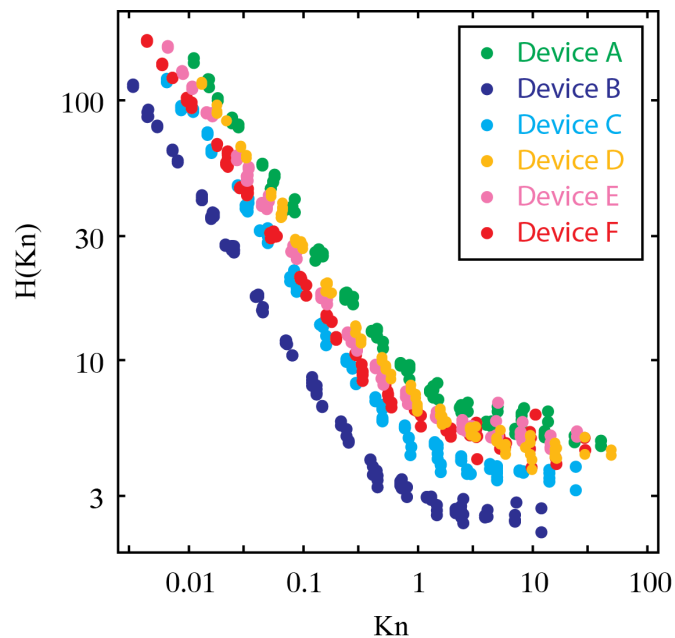


**Figure S9:** Scaled quality factor  $H(Kn)$  for all cantilever devices in Figure S8, plotted in a single graph to highlight variations as a function of device geometry.

## REFERENCES

- [1] J. E. Sader, J. Pacifico, C. P. Green and P. Mulvaney, General scaling law for stiffness measurement of small bodies with applications to the atomic force microscope. *Journal of Applied Physics*, **97**, 124903 (2005).
- [2] J. E. Sader, J. A. Sanelli, B. D. Adamson, J. P. Monty, X. Wei, S. A. Crawford, J. R. Friend, I. Marusic, P. Mulvaney and E. J. Bieske, Spring constant calibration of atomic force microscope cantilevers of arbitrary shape. *Review of Scientific Instruments*, **83**, 103705 (2012).
- [3] P. W. Bridgman, *Dimensional Analysis* (Yale University Press, New Haven, 1931).
- [4] D. Rugar, H. J. Mamin, R. Erlandsson, J. E. Stern, and B. D. Terris. Force microscope using a fiber-optic displacement sensor. *Review of Scientific Instruments*, **59**, 2337-2340 (1988).
- [5] R. E. Fischer and B. Tadic-Galeb. *Optical system design*. McGraw Hill, New York, 2000.
- [6] K. L. Ekinici, Y. T. Yang, and M. L. Roukes. Ultimate limits to inertial mass sensing based upon nanoelectromechanical systems. *Journal of Applied Physics*, **95**, 2682-2689 (2004).
- [7] J. E. Sader, I. Larson, P. Mulvaney, and L. R. White. Method for the calibration of atomic force microscope cantilevers. *Review of Scientific Instruments*, **66**, 3789-3798 (1995).
- [8] R. A. Bidkar, R. C. Tung, A. A. Alexeenko, H. Sumali, and A. Raman. Unified theory of gas damping of flexible microcantilevers at low ambient pressure. *Applied Physics Letters*, **94**, 163117 (2009).
- [9] W. E. Newell. Minaturization of tuning forks. *Science*, **161**, 1320-1326 (1968).
- [10] G. A. Bird. *Molecular gas dynamics and the direct simulation of gas flows*. Clarendon Press, Oxford, 1994. [Eq. 7.70 on p. 170].
- [11] J. E. Sader. Frequency response of cantilever beams immersed in viscous fluids with applications to the atomic force microscope. *Journal of Applied Physics*, **84**, 64-76, (1998).